




Article

Composites Based on Electrodeposited WO₃ and TiO₂ Nanoparticles for Photoelectrochemical Water Splitting

Ramunas Levinas ^{1,2,*} , Elizabeth Podlaha ^{3,*}, Natalia Tsyntsaru ^{1,4}  and Henrikas Cesiulis ¹ 

¹ Faculty of Chemistry and Geosciences, Vilnius University, Naugarduko Str. 24, LT-03225 Vilnius, Lithuania; natalia.tintaru@chf.vu.lt (N.T.); henrikas.cesiulis@chf.vu.lt (H.C.)

² State Research Institute, Center for Physical Sciences and Technology (FTMC), Saulėtekio Ave. 3, LT-10257 Vilnius, Lithuania

³ Department of Chemical and Biomolecular Engineering, Clarkson University, 8 Clarkson Ave., Potsdam, NY 13699, USA

⁴ Institute of Applied Physics, Moldova State University, MD-2028 Chisinau, Moldova

* Correspondence: ramunas.levinas@ftmc.lt (R.L.); epodlaha@clarkson.edu (E.P.)

Abstract: Photoelectrochemically active WO₃ films were fabricated by electrodeposition from an acidic (pH 2), hydrogen-peroxide-containing electrolyte at −0.5 V vs. SCE. WO₃-TiO₂ composites were then synthesized under the same conditions, but with 0.2 g/L of anatase TiO₂ nanoparticles (⊙ 36 nm), mechanically suspended in the solution by stirring. After synthesis, the films were annealed at 400 °C. Structural characterization by XRD showed that the WO₃ films exhibit the crystalline structure of a non-stoichiometric hydrate, whereas, in WO₃-TiO₂, the WO₃ phase was monoclinic. The oxidation of tungsten, as revealed by XPS, was W⁶⁺ for both materials. Ti was found to exist mainly as Ti⁴⁺ in the composite, with a weak Ti³⁺ signal. The efficiency of the WO₃ films and composites as an oxygen evolution reaction (OER) photo-electrocatalyst was examined. The composite would generate approximately three times larger steady-state photocurrents at 1.2 V vs. SCE in a neutral 0.5 M Na₂SO₄ electrolyte compared to WO₃ alone. The surface recombination of photogenerated electron–hole pairs was characterized by intensity-modulated photocurrent spectroscopy (IMPS). Photogenerated charge transfer efficiencies were calculated from the spectra, and at 1.2 V vs. SCE, were 86.6% for WO₃ and 62% for WO₃-TiO₂. Therefore, the composite films suffered from relatively more surface recombination but generated larger photocurrents, which resulted in overall improved photoactivity.

Keywords: tungsten trioxide titania composite; electrodeposition; photoelectrochemical water splitting; IMPS of OER



Citation: Levinas, R.; Podlaha, E.; Tsyntsaru, N.; Cesiulis, H. Composites Based on Electrodeposited WO₃ and TiO₂ Nanoparticles for Photoelectrochemical Water Splitting. *Materials* **2024**, *17*, 4914.

<https://doi.org/10.3390/ma17194914>

Academic Editor: Giovanni Sotgiu

Received: 22 August 2024

Revised: 17 September 2024

Accepted: 27 September 2024

Published: 8 October 2024



Copyright: © 2024 by the authors. Licensee MDPI, Basel, Switzerland. This article is an open access article distributed under the terms and conditions of the Creative Commons Attribution (CC BY) license (<https://creativecommons.org/licenses/by/4.0/>).

1. Introduction

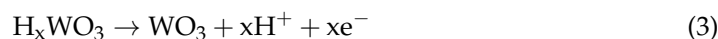
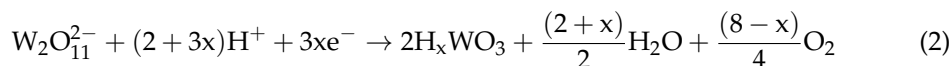
The adverse environmental impact of using fossil fuels for energy needs and generating H₂ for chemical processing has led to significant research toward finding alternative and sustainable energy carriers, such as hydrogen (H₂), with H₂ produced by solar water splitting is more advantageous compared to other forms of green hydrogen [1–3]. The photoelectrochemical (PEC) water-splitting process includes light harvesting, photogenerated charge separation, and surface catalysis, and is an effective strategy as an alternative to fossil fuels. The reduction of water to produce hydrogen is coupled with the more kinetically hindered oxygen evolution reaction, which is typically carried out on metal oxide photoanodes [4,5]. Although TiO₂ is recognized as an effective inexpensive photocatalyst in the UV range, [6,7], the addition of tungsten trioxide (WO₃) is widely known to lower the band gap (~2.75 eV) and hence, allows absorption to occur within the visible range of the solar spectrum, [8–11]. However, WO₃ alone suffers from high recombination of photon-generated electron–hole pairs [12] and is susceptible to photocorrosion caused by peroxo-species formed on the surface during the photoelectrochemical reaction [13]. Tungsten trioxide doped by TiO₂ shows a red-shifted optical response in the visible light

range due to a band gap decrease from a lowering of the conduction band edge, and can act as a photocatalyst. Momeni and Nazari [14] reported a change in band gap from 3.23 eV for bare TiO₂ to 2.78 eV for WO₃-doped TiO₂ nanotubes. Also, doping TiO₂ with cations like tungsten (W⁶⁺) introduces energy levels in TiO₂ just below the conduction band that acts as an electron trap increasing the lifetime of charge carriers, and thus retarding recombination [15].

Heterojunctions of WO₃/TiO₂ layers have been used to increase the efficiency of the photocatalysts [16–20] by aligning the band structures of the two coupled semiconductors to encourage migration of photogenerated electrons (e[−]) and holes (h⁺) in separate directions across the heterojunction boundary, which reduces the electron–hole recombination. The highly oxidative valence band of WO₃, arising from the O 2p orbitals, also helps to drive oxidation reactions, such as PEC oxygen evolution or degradation of dyes. WO₃/TiO₂ composites have been reported to perform as stable and efficient photoanodes in water splitting [21–23]. Numerous reports of dye degradation with tungsten doped TiO₂ or heterojunctions are reported through the reactions of a photogenerated superoxide [24–28]. One such heterojunction unique to electrodeposition is the work presented by Martin et al. [29]. They electrodeposited WO₃ onto a metallic Ti electrode then heat treated it to create a WO₃/TiO₂/Ti layered material that exhibited high photocurrent values toward the photoelectrocatalytic degradation of propyl paraben. An alternative strategy to reduce recombination rates is to apply a potential or bias and photogenerated electrons are drawn away from the electrode–electrolyte interface through the external surface. This electrically enhanced photocatalysis was observed for electrochemically prepared TiO₂/WO₃ layers on stainless steel for the oxidation of organics [30].

Nanostructuring is also important for generating quantum confinement effects that alter the electron and hole transport behaviors, shifting of the electronic band structure, and the large surface-to-volume ratio can significantly increase the surface reaction sites [31]. However, it can also introduce defects or additional grain boundaries that can promote recombination [32].

As mentioned, synergistic effects, as a result of combining different photoactive materials, provide a promising pathway to improve the photoelectrochemical performance in heterojunction devices for solar water splitting [33]. To this end, a nanocomposite WO₃-TiO₂ film was electrodeposited with a WO₃ matrix incorporating nanoparticles of TiO₂, in contrast to layered materials or those with a matrix of TiO₂. The electrodeposition of WO₃ films followed the approach by Pauporté [34], where the electrochemical deposition mechanism is multistaged and occurs through the reduction of a peroxy-tungstate species as outlined in Equations (1) to (3) [35–37].



In this study, the approach is modified by adding TiO₂ nanoparticles to the sodium tungstate–hydrogen peroxide electrolyte. The electrodeposition is then carried out to simultaneously electrodeposit a WO₃ film and capture TiO₂ nanoparticles, resulting in a one-step synthesis of a composite with improved photoactivity for water splitting. Moreover, the use of an advanced non-stationary photoelectrochemical technique (IMPS) is demonstrated to probe charge carrier photogeneration in the space-charge layer and to elucidate important kinetic constants for charge transfer and recombination.

2. Materials and Methods

2.1. Composite Electrodeposition

A schematic representation of the cell and process used to deposit WO₃ and WO₃-TiO₂ films is shown in Figure 1. All used chemicals were of ACS reagent grade. The electrolyte

to electrodeposit WO_3 films was prepared from 0.025 M $\text{Na}_2\text{WO}_4 \cdot 2\text{H}_2\text{O}$ (Fisher Chemical, Hampton, NH, USA), 0.075% (v/v) H_2O_2 (Fisher Chemical, Hampton, NH, USA) which was 1.25 mL of 30% hydrogen peroxide, and the pH was adjusted to 1.4 with sulfuric acid (Fisher Chemical, Hampton, NH, USA). To electrodeposit composite $\text{WO}_3\text{-TiO}_2$ films, the same electrolyte composition was used, but additionally, a particle loading of 0.2 g/L of anatase TiO_2 (Thermo Fisher Scientific, Waltham, MA, USA) of average ϕ 36 nm was added. The nanoparticles were mechanically suspended in the electrolyte by using a magnetic stir bar. Electrodeposition was carried out in a three-electrode cell, with a stainless-steel (type 316) working electrode (plates of 2 cm \times 2 cm dimensions were used as the substrate, with a circular working area of 1.226 cm²), a Pt counter electrode, and an SCE reference electrode. The substrate was positioned in a holder parallel to the bottom of the electrodeposition bath. Deposition occurred during an applied potential of -0.5 V vs. SCE for 5 min.

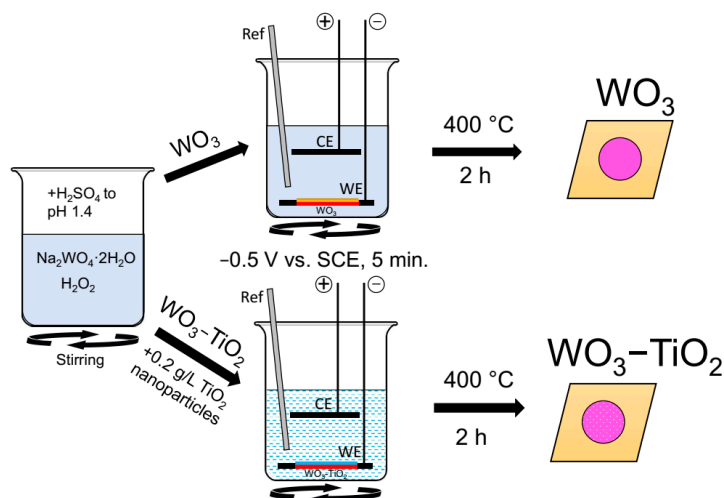


Figure 1. Schematic representation of material synthesis and annealing process.

2.2. Structural and Surface Morphology Characterization

The as-deposited WO_3 and $\text{WO}_3\text{-TiO}_2$ films were thermally annealed at 400 °C for two hours, with a 2 °C min⁻¹ temperature ramp-up rate. The surface morphology was characterized by a Hitachi TM 3000 scanning electron microscope (Hitachi Ltd., Tokyo, Japan). XRD diffraction patterns were obtained with a Rigaku MiniFlex II x-ray diffractometer (Rigaku Corporation, Tokyo, Japan).

The XPS analyses were carried out with a Kratos Axis Supra spectrometer (Kratos Analytical Limited, Manchester, UK), using a monochromatic Al K(alpha) source (15 mA, 15 kV). Survey scan analyses were carried out on the area of 300 \times 700 μm at a pass energy of 160 eV. High-resolution analyses were also carried out on the area of 300 \times 700 μm , but at a pass energy of 20 eV. The XPS signal due to adventitious carbon located at 284.8 eV was used as a binding energy (BE) reference.

2.3. PEC Characterization

The photoelectrochemical response of the resulting deposits was examined with linear sweep voltammetry, chronoamperometry, and IMPS, using a ZAHNER Zennium CIMPS-QE/IPCE system (Zahner-Elektrik, Kronach, Germany). The photoelectrochemical cell included a quartz window for front-illumination of the films, a platinum counter electrode, and an SCE reference electrode. A neutral 0.5 M Na_2SO_4 electrolyte was used. The light source was a variable-intensity LED, emitting monochromatic 365 nm UV light.

A typical characterization procedure of an electrochemically deposited and annealed WO_3 or $\text{WO}_3\text{-TiO}_2$ film consisted of these steps:

Voltammetry experiments were conducted from 0.2 V to 1.6 V (vs. SCE) at 5 mV s⁻¹, with a 4-s on/off illumination pulse (2 s on/2 s off). Chronoamperometry at a constant

potential of 1.2 V used an illumination pulse of 120 s (60 s on/60 s off). Light intensity was set to 30 mW cm^{-2} . IMPS was measured at steady state potentials: 0.6 V, 0.8 V, 1.0 V, 1.2 V (100 mW cm^{-2} light intensity, 10% amplitude modulation, 10 kHz to 0.1 Hz).

3. Results and Discussion

3.1. Structure and Surface Morphology

Figure 2 shows the XRD patterns of electrodeposited WO_3 and $\text{WO}_3\text{-TiO}_2$ films that had been annealed at 400°C for 2 h. The XRD pattern of the annealed stainless steel substrate is also included. It contains two peaks characteristic of austenite iron (JCPDS No. 00-023-0298) at 43.5° and 50.7° , and the substrate peaks also emerge in the diffractograms of the deposited films. The diffractograms of WO_3 and $\text{WO}_3\text{-TiO}_2$ reveal the radically different phase structure of the films. $\text{WO}_3\text{-TiO}_2$ displays all the characteristic peaks of monoclinic WO_3 [38,39]. However, there are a couple of relatively low-intensity peaks that cannot be attributed to this phase, in particular, at 27.6° and 49.5° . The analysis of WO_3 reveals the origin of these peaks. The diffractogram of WO_3 contains a very intense peak at $\sim 24.1^\circ$, which may correspond to the (200) face of monoclinic WO_3 . There is also a broad hump at a slightly lower 2θ of 23.3° , and two small peaks at 27.8° and 49.5° . These reasonably correspond to the unidentified peaks from $\text{WO}_3\text{-TiO}_2$ and have been attributed to hydrated forms of WO_3 in the literature [40,41]. It is claimed that the formation of $\text{WO}_3 \cdot x\text{H}_2\text{O}$ can occur through tuning of the intermediate peroxo-complex and thus is related to the H_2O_2 content in the solution [40]. The electrodeposition of a hydrated tungsten oxide has also recently been reported under conditions very similar to those used in this study [42]. Therefore, the formation of monoclinic WO_3 when electrodepositing the composite must have been related to an equilibrium shift in the intermediate peroxo-complex caused by the interaction of solution species with nanoparticulate TiO_2 , possibly solvation. The crystallite sizes of WO_3 , as approximated by the Scherer equation, are $41 \pm 9 \text{ nm}$ for WO_3 and $27.4 \pm 3.3 \text{ nm}$ for $\text{WO}_3\text{-TiO}_2$. Regarding the presence of TiO_2 , in the diffractogram of the composite film, a very faint hump at $\sim 25^\circ$ can perhaps be distinguished, which could be related to the main (101) peak of anatase TiO_2 .

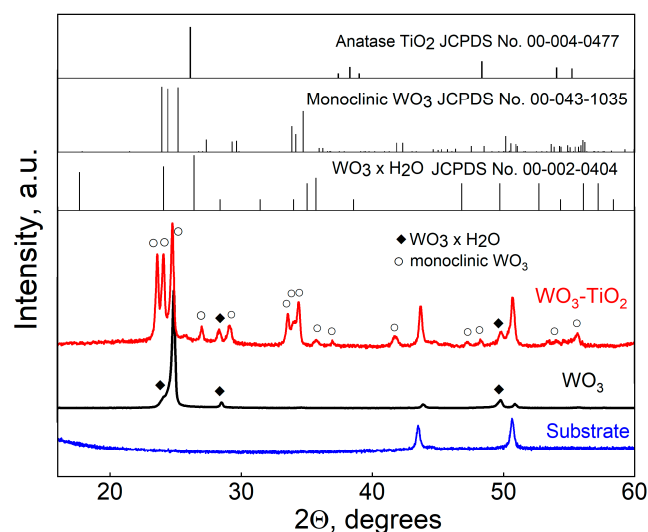


Figure 2. XRD patterns of stainless steel substrate and electrodeposited WO_3 and $\text{WO}_3\text{-TiO}_2$ composite films, after annealing at 400°C .

The visual appearance and SEM surface morphology images of WO_3 and $\text{WO}_3\text{-TiO}_2$ films are shown in Figure 3. The WO_3 film (Figure 3a) is inhomogeneously polychromic, which is indicative of a compact thin film of slightly varying thicknesses. The surface morphology, as observed by SEM, is smooth and fine-grained, as was also observed by Pauporté when first reporting on WO_3 electrodeposition by this method [34]. For both films, signs of emerging cracks can be seen. It was noted earlier [43,44] that cracking and

delamination occur if the layer is thicker (i.e., after longer deposition times). Accordingly, the $\text{WO}_3\text{-TiO}_2$ film is already cracked (Figure 3b), which may indicate a larger thickness. Scattered agglomerates of white particles, which are most likely TiO_2 , can be observed on the surface. Visually, the film appears “cloudy” because TiO_2 particles had settled at the surface of the film during deposition. These particles were not always well-adhered to the surface. If the electrodeposition time was prolonged, they would detach from the surface when immersed in an electrolyte for further characterization. For this reason, the PEC characterization was carried out on films that had been deposited for 5 min.

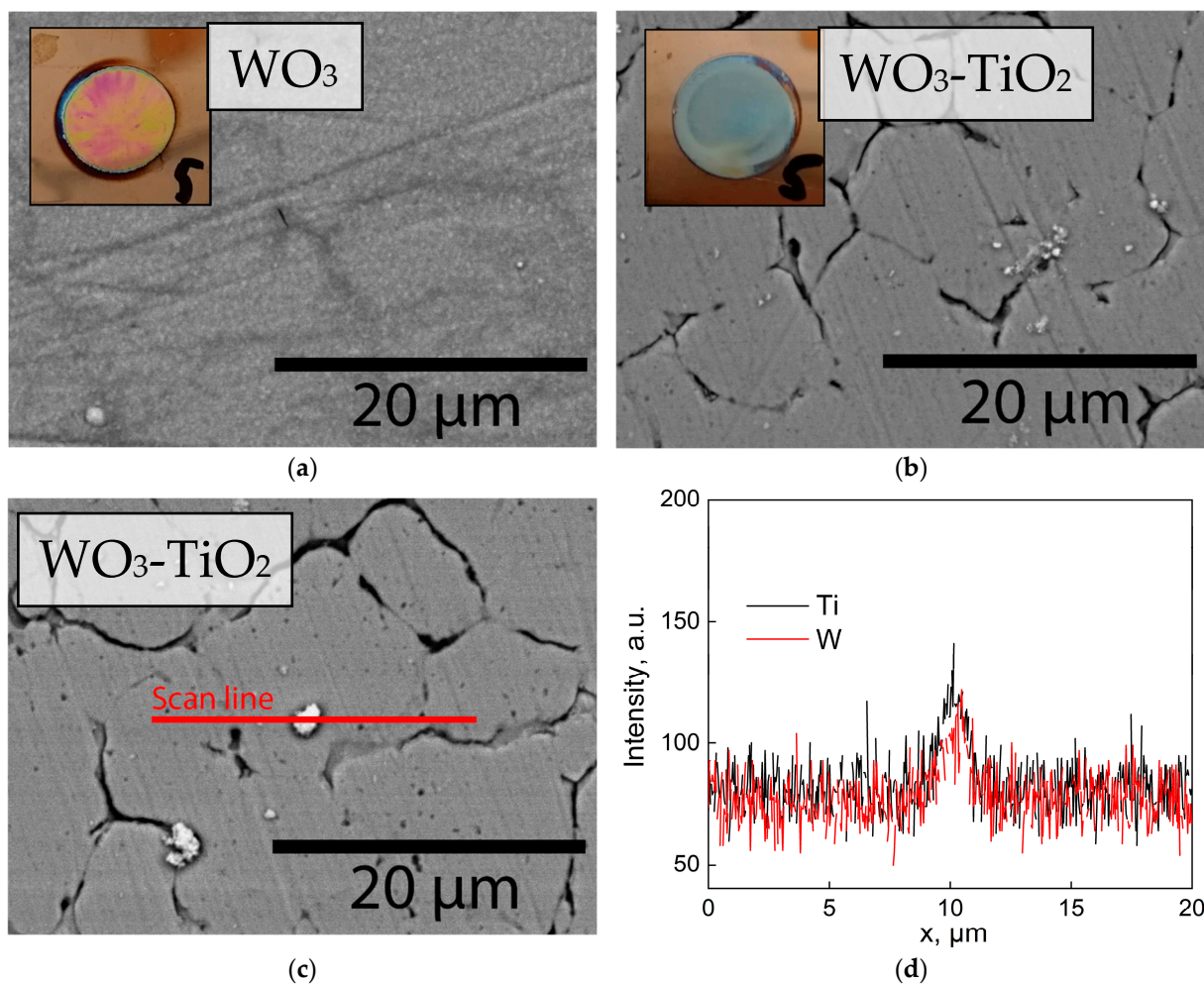


Figure 3. SEM surface morphology images of (a) WO_3 ; (b) $\text{WO}_3\text{-TiO}_2$ films electrodeposited for 5 min, (c) SEM image of EDX line scan on a $\text{WO}_3\text{-TiO}_2$ film, (d) EDX line scan data portraying titanium and tungsten signals.

The results of an EDX line scan (Figure 3c,d) show that a TiO_2 nanoparticle agglomeration was observed on the surface. Titanium was detected, albeit with a very weak signal. It is also interesting to note that the tungsten signal increases along with titanium. This may simply be a topographical effect (i.e., a stronger signal obtained from a point closer to the detector), but it could also indicate that WO_3 had electrodeposited onto TiO_2 .

The near-surface electronic structure of the WO_3 and $\text{WO}_3\text{-TiO}_2$ films was investigated by XPS. It was found that for both films, the core-level structure of W 4f deconvolutes into a single doublet with W $4f_{7/2}$ and W $4f_{5/2}$ peaks at binding energies of 35.46 eV and 37.6 eV, respectively (Figure 4a,b). The position of these peaks, and the spin-orbit splitting energy of 2.14 eV, indicate the total dominance of the W^{6+} oxidation state [45,46]. Interestingly, the O 1s core-level spectra reveal that oxygen can be found in at least two oxidation states

(Figure 4c,d). The O 1s peak seen here at 530.22 eV for WO_3 and 530.48 eV for $\text{WO}_3\text{-TiO}_2$ is commonly attributed to lattice oxygen (i.e., the W-O bond) [47].

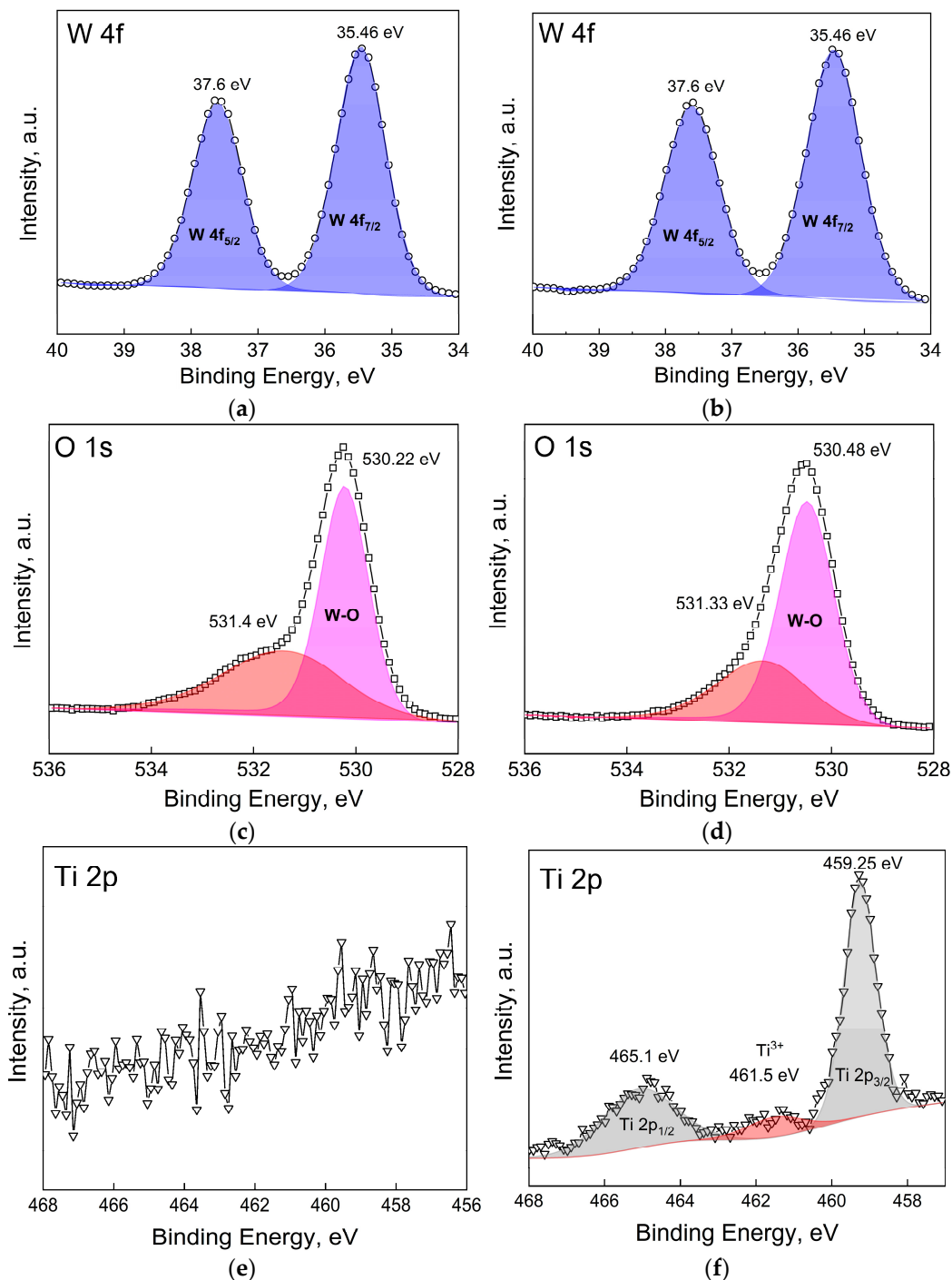


Figure 4. Deconvoluted core-level XPS spectra of W 4f, O 1s, and Ti 2p of a WO_3 film (a,c,e) and $\text{WO}_3\text{-TiO}_2$ film (b,d,f).

The origin of the second much broader peak at ~ 531.4 eV is slightly more complicated to explain. First and foremost, this cannot be Ti-related O because (1) the lattice oxygen peak energy is expected to be around 529–530 eV [48] and (2) the same peak also exists for WO_3 without TiO_2 . A couple of other possibilities that are often reported are oxygen from non-stoichiometric WO_{3-x} or -OH groups incorporated within the lattice, which can result in peaks in the O 1s spectra at approximately 532.5 eV [47,49]. However, these energies also do not match. A very recent work by T. J. Frankcombe and Y. Liu describes what is

most likely the cause of these peaks [50]. They found that a peak at this energy (commonly ascribed in the literature to oxygen vacancies) is instead caused by O 1s electrons from water molecules that are chemisorbed to the surface or surface oxygen passivated by hydrogen. This agrees well with the W 4f spectra, which show 100% dominance of W^{6+} and no trace of reduced oxidation states that would be expected with a large number of oxygen vacancies. The existence of chemisorbed water may also be related to the observation of hydrates in XRD characterization (Figure 2). Lastly, no Ti is found on WO_3 , and only a very weak Ti 2p signal is obtained from the WO_3 - TiO_2 film (Figure 4e,f). The core level spectrum deconvolutes into one doublet with peaks at 459.25 eV and 465.1 eV, corresponding to Ti^{4+} from anatase TiO_2 [51]. An indistinct hump at 461.5 eV may also be observed. It is on the verge of being noise, but a peak at this position has been attributed to Ti^{3+} [52]. The reduction of titanium dioxide nanoparticles is feasible under cathodic conditions in an acidic electrolyte, so the signal is attributed to Ti^{3+} here as well.

3.2. Photoelectrochemical Characterization

Initially, the PEC properties of WO_3 and WO_3 - TiO_2 films were characterized by carrying out a potential scan with intermittent on/off light pulses (Figure 5a). Two differences are immediately apparent: (1) the WO_3 - TiO_2 film generates larger photocurrents throughout the entire potential range and (2) the photocurrent onset potential of the composite is more cathodic (~ 0.2 V vs. SCE) in comparison to just WO_3 (~ 0.35 V vs. SCE). As expected, the magnitude of the photocurrent increases with the applied potential as the space-charge layer, where the photoexcitation of charge carriers occurs and becomes wider due to the increasing strength of the applied electrical field. It is also worth noting that both WO_3 and WO_3 - TiO_2 films show an appreciable amount of surface hole recombination, which is evident from the initial photocurrent overshoot that occurs at the instant light is turned on.

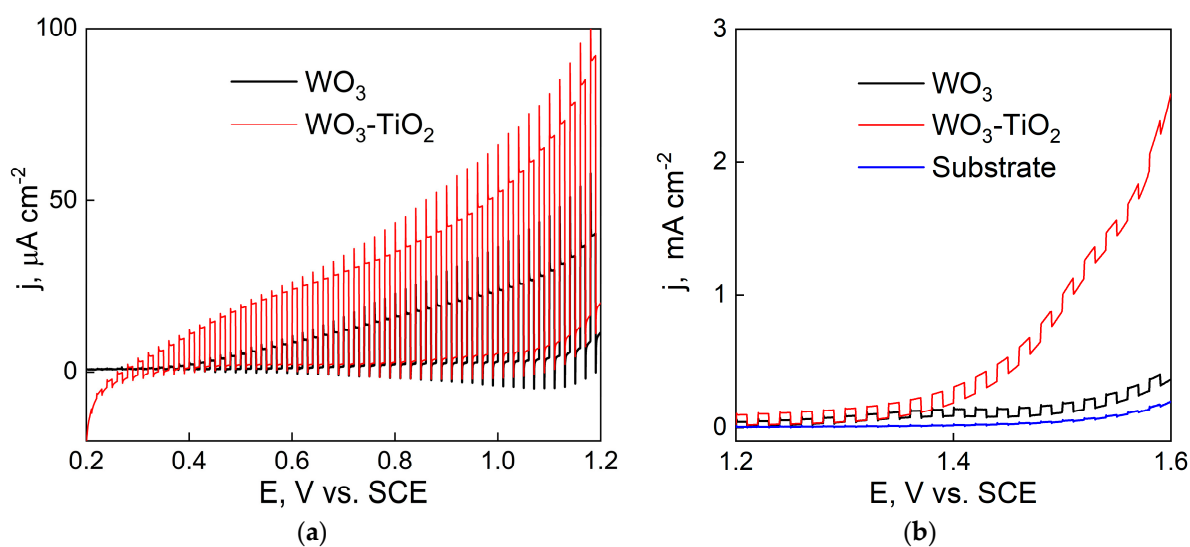


Figure 5. Chopped UV LSV measurements at low potentials (a) and high potentials (b) in 0.5 M Na_2SO_4 of WO_3 and WO_3 - TiO_2 films deposited within 5 min; 5 mV s^{-1} , 30 mW cm^{-2} light intensity.

An additional difference between the activities of these films is noted at higher applied potentials of $\geq \sim 1$ V vs. SCE, which roughly corresponds to 1.23 V vs. RHE in neutral pH (Figure 5b). In this case, particularly for WO_3 - TiO_2 , the electrochemical current rises sharply and is most probably attributable to the onset of electrochemical water splitting/oxygen evolution (OER). A similar effect, although with much lower current densities, is observed for the annealed stainless steel substrate. Thus, the composite films exhibit better electrochemical OER activity. This may simply be an effect of increased surface area [53] or the improved OER mechanistic kinetics of WO_3 [54].

Because the profile of the photocurrent pulse provides useful information about the material photoactivity and surface recombination [55], potentiostatic photocurrent pulses were obtained at 1.2 V vs. SCE and with a longer on/off cycle duration of 120 s (Figure 6). This made it possible to observe the initial photocurrent overshoot immediately upon turning on the light, and the subsequent decay over several pulses.

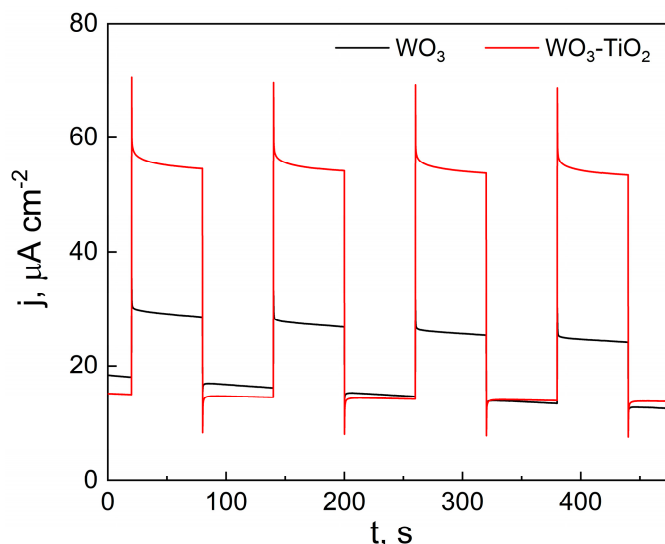


Figure 6. UV on/off pulses in 0.5 M Na₂SO₄ of WO₃ and WO₃-TiO₂ films; 365 nm LED, 30 mW cm⁻² light intensity.

At the moment the light is turned on, the photocurrent density ($j_{t=0}$) is proportional to the maximum amount of photogenerated electron–hole pairs. For a photoanode, the electrons move to the back contact and are registered as photocurrent, and the holes move toward the electrode–electrolyte interface, where they are either lost to surface recombination or are transferred into the electrolyte to carry out an oxidative photoelectrochemical reaction. After this, the photocurrent decays until a steady state value (j_{ss} is assumed to be the photocurrent at the end of the 60 s pulse) is reached. In this case, it is observed that the WO₃-TiO₂ film displays slightly more relative surface recombination than WO₃. For example, for the WO₃ film, the $j_{ss}/j_{t=0}$ ratio is 0.8; whereas, for the comparable composite film, it is lower at 0.77. However, the WO₃-TiO₂ film also generates larger photocurrents overall (~40 $\mu\text{A cm}^{-2}$ compared to just under 12 $\mu\text{A cm}^{-2}$ for WO₃). A similar result was observed by Castro et al., who found that a hydrothermally synthesized WO₃ composite with 40 wt% of TiO₂ exhibited larger photocurrents than WO₃ [21]. Similarly, WO₃/TiO₂ heterostructures on reduced graphene oxide were shown to generate significantly larger photocurrents than the plain films alone [22].

Lastly, similar to the initial jump, there is an “overshoot” to the downside when illumination is turned off. This occurs because of the recombination of holes trapped on the surface with electrons—a phenomenon similar to the decay of the photocurrent.

3.3. IMPS Study

IMPS is a non-stationary photoelectrochemical analysis method, modeled by Ponomarev and Peter [56], to determine the features of the space charge region relative to the reaction rate constants. A sinusoidal modulation is applied to the intensity of illumination, and the working electrode under investigation is kept at potentiostatic conditions. In this case, the (photo)current response is proportional entirely to the incident photon flux, i.e., conversion efficiency. It must be noted that here, the light intensity was increased in comparison to previous experiments (30 mW cm⁻² to 100 mW cm⁻²). This is because the signal for IMPS is not obtained from the entire photocurrent, but from the light-perturbation-induced photocurrent, which corresponds to the photocurrent generated

by the amplitude of light intensity modulation (10%). If this light intensity is too low (e.g., 3 mW cm^{-2} as 10% of 30 mW cm^{-2}), the spectra can be noisy. However, photogenerated charge carrier recombination is generally larger at higher light intensities [57], so care should be taken to find the optimal measurement conditions for a particular system.

IMPS Nyquist spectra obtained for WO_3 are shown in Figure 7, where H represents the complex transfer function of the resulting current measured by controlling the light intensity, normalized to the geometric electrode area. The first quadrant reflects the response from charge-transfer kinetic and surface recombination. The low-frequency intercept H'_{LF} (left side) when $H'' \rightarrow 0$ represents the differential steady-state photocurrent increase due to a differential increase in the light intensity and should be zero if no photoelectrochemical reactions occur. ω_{LF} , the radial frequency of the highest point of the recombination semicircle, is a product of first-order rate constants of photogenerated charge transfer and recombination and is inversely related to the recombination time constant.

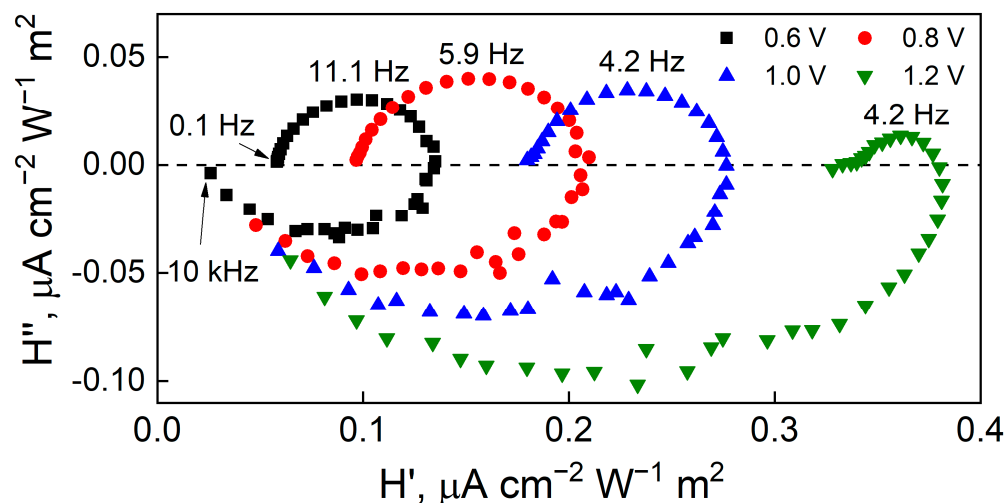


Figure 7. Nyquist plots for IMPS of a WO_3 film that had been electrodeposited for 5 min, obtained in $0.5 \text{ M Na}_2\text{SO}_4$, 365 nm LED , 100 mW cm^{-2} light intensity with 10% modulation amplitude.

Figure 7 for WO_3 shows a non-zero H'_{LF} , suggesting that an electrochemical reaction occurs at all applied potentials. In Figure 8 for $\text{WO}_3\text{-TiO}_2$ at 0.6 and 0.8 V, this intercept is nearly zero and thus, electron–hole generation and surface recombination primarily occur. A significant shift in this intercept occurs at 1 V where a significant amount of OER is expected to commence driven by the applied potential. The intercept when the imaginary part is zero at a higher frequency (right side) represents the amplitude of the flux of charge carriers to the surface. This intercept occurs at a value of H' that can be expressed as Equation (4).

$$H' = j_h \frac{C_H}{C_H + C_{\text{SC}}} \quad (4)$$

where j_h is the hole current amplitude, C_H and C_{SC} are the Helmholtz and space charge layer capacitances, respectively.

Since the Helmholtz layer size is typically smaller than the width of the depletion, the space charge layer, then it is expected that the Helmholtz capacitance is higher, $C_H > C_{\text{SC}}$ [58]. Then, this intercept equals j_h , i.e., the hole current. At higher frequencies relative to this intercept, the influence of the capacitance of the semiconductor space charge dominates and the response moves to the lower quadrant, with a negative imaginary transfer function. The discussed parameters that had been obtained from the spectra are presented in Table 1. The overall trend is that, as the applied potential is raised, H'_{LF} increases because more photogenerated holes are transferred as surface recombination is suppressed. Moreover, the IMPS spectra are not normalized to the amplitude of the photogenerated hole current, and therefore, larger IMPS spectra magnitudes of $\text{WO}_3\text{-TiO}_2$

suggest higher conversion efficiencies overall, corresponding well to LSV and potentiostatic pulse data.

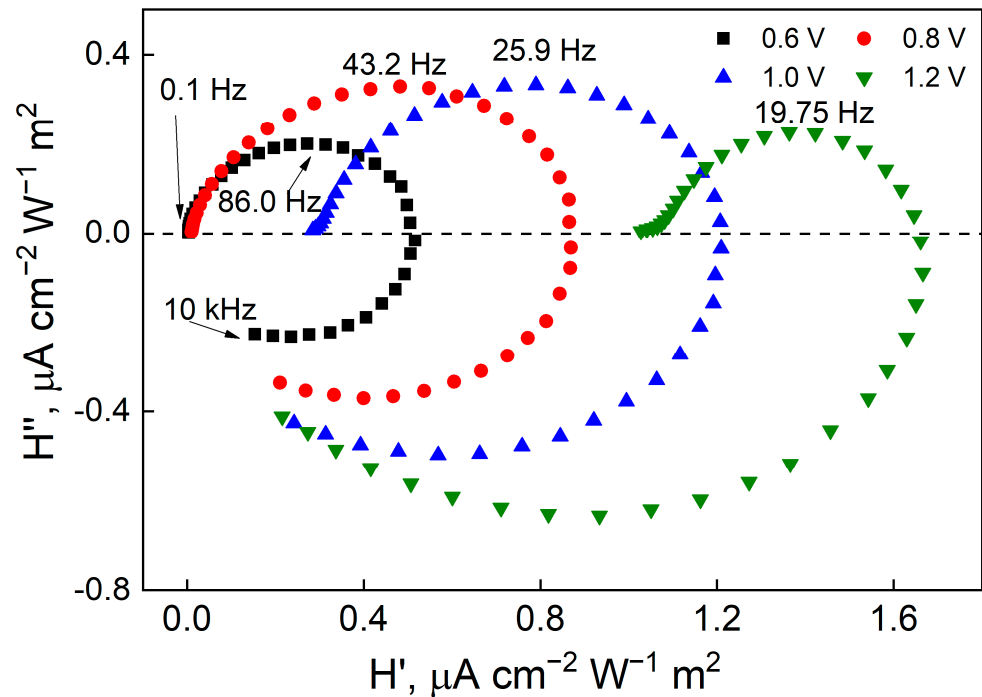


Figure 8. Nyquist plots for IMPS of a $\text{WO}_3\text{-TiO}_2$ film that had been electrodeposited for 5 min, obtained in $0.5\text{ M Na}_2\text{SO}_4$, 365 nm LED , 100 mW cm^{-2} light intensity with 10% modulation amplitude.

Table 1. Parameters, obtained from interpretation of IMPS Nyquist plots.

E, V	WO_3			$\text{WO}_3\text{-TiO}_2$		
	ω_{LF} , Rad s ⁻¹	H'_{LF} , $\mu\text{A cm}^{-2}$ $\text{W}^{-1}\text{ m}^2$	j_h , $\mu\text{A cm}^{-2}$ $\text{W}^{-1}\text{ m}^2$	ω_{LF} , Rad s ⁻¹	H'_{LF} , $\mu\text{A cm}^{-2}$ $\text{W}^{-1}\text{ m}^2$	j_h , $\mu\text{A cm}^{-2}$ $\text{W}^{-1}\text{ m}^2$
0.6	69.6	0.058	0.135	546.2	0.004	0.511
0.8	37.0	0.097	0.208	271.3	0.010	0.867
1.0	26.4	0.180	0.276	162.7	0.284	1.208
1.2	26.4	0.330	0.378	124.0	1.028	1.653

In IMPS spectra, the high-frequency semicircle occurs because of the RC time constant of the electrochemical cell, i.e., the series resistance of the substrate and the total capacitance. Conversely, the low-frequency semicircle describes the recombination and charge transfer kinetics. Kinetically, these processes are described by first order rate constants: k_{tr} —the rate constant of charge transfer across this same interface and k_{rec} —the rate of electron–hole recombination at the semiconductor/electrolyte interface. The spectra shown in Figures 5 and 6 exhibit some characteristic tendencies. Most notably—the radius of the low frequency semicircle decreases as the applied potential is increased. In IMPS, the value of the low frequency intercept H'_{LF} corresponds to the DC photocurrent, scaled by the 10% modulation, and is expressed as Equation (5).

$$H'_{\text{LF}} = j_h \frac{k_{\text{tr}}}{k_{\text{tr}} + k_{\text{rec}}} \quad (5)$$

Here, $k_{\text{tr}}/k_{\text{tr}} + k_{\text{rec}}$ corresponds to η_{trans} —the fraction of hole flux from the space charge region that is involved in the charge transfer reaction, or the transfer efficiency. The transfer efficiency increases with applied potential as photogenerated charge carriers

can participate in an electrochemical reaction. Therefore, electron–hole recombination is significant at less positive potentials (the low frequency intercept value is closer to 0), because there is no electrochemical reaction, but at 1.2 V, it decreases considerably with the occurrence of OER.

Several important parameters can be calculated from IMPS spectra. Firstly, the transfer efficiency is an indicator of how many of the holes that had arrived at the semiconductor/electrolyte interface that were transferred into the electrolyte to provide the photoelectrochemical reaction. The data for WO₃ and WO₃-TiO₂ films are shown in Figure 9. As expected, the efficiencies are larger with increasing applied potential. Plain WO₃ films have larger photogenerated transfer efficiency over the entire measured potential range, while the TiO₂-containing composites have total recombination at lower potentials, but improve rapidly at higher potentials.

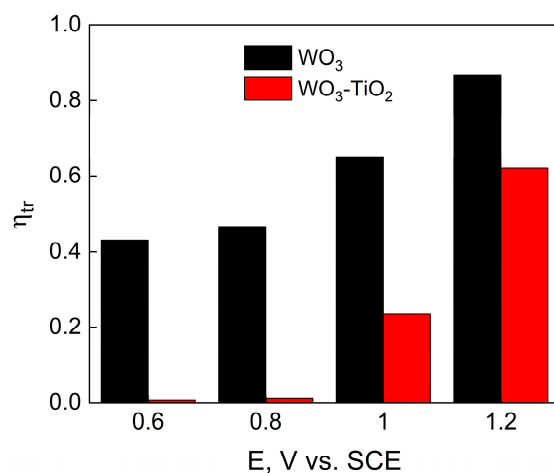


Figure 9. Transfer efficiency values, obtained from IMPS spectra for WO₃ and WO₃-TiO₂ films.

To fully discern reaction kinetics, the rate constants should be considered. Both k_{tr} and k_{rec} can be calculated from two characteristic points of the IMPS spectrum: the low frequency intercept H'_{LF} (Equation (5)) and ω_{LF} , the radial frequency of the highest point of the recombination semicircle, which is described by Equation (6).

$$\omega_{LF} = k_{tr} + k_{rec} \quad (6)$$

The spectra were analyzed and the rate constants are presented in Figure 10 in relation to applied potential. Firstly, it can be seen that for both measured photoelectrodes, k_{rec} decreases with applied potential (Figure 10a), which is expected from the added potential bias as has been discussed earlier.

The k_{rec} values of WO₃-TiO₂ are larger, showing faster recombination kinetics. However, when considering the kinetic transfer constant, it is apparent that k_{tr} increases significantly for the composite films at higher potentials, compared to WO₃ (Figure 10b). Thus, there is a higher OER reaction rate on the WO₃-TiO₂ under a biased photoelectrochemical environment. At an applied potential of 1.2 V vs. SCE, the k_{tr} of the composite is three times larger than that of the respective WO₃ film, consistent with the voltammetry result in Figure 5 and the chronoamperometry in Figure 6.

While the addition of discrete TiO₂ nanoparticles to WO₃ generated a higher photocurrent compared to WO₃ alone, it had the negative effect of increasing the recombination rate constant, particularly near open circuit conditions at small applied potentials. The increased recombination rate may be due to the introduction of grain boundaries and local potential perturbation by the particles. The recombination rate constant decreased with applied potential, and in the applied potential range for conventional electrolysis, the WO₃-TiO₂ composite greatly exceeded the performance of the WO₃. At an even larger applied potential exceeding 1.2 V vs. SCE, evident in the polarization curve in Figure 5, the WO₃-TiO₂

composite OER current density greatly exceeded WO_3 even without light; thus, the TiO_2 addition to WO_3 improved its electrocatalytic performance. Georgieva et al. [30] also found an enhanced photocatalysis for TiO_2/WO_3 layers on stainless steel compared to WO_3 but attributed the enhancement to reduced recombination. The results presented here are in contrast to this reasoning, elucidated by the additional evidence from IMPS. The enhancement in our work is due to larger charge transfer kinetics and not suppressed recombination.

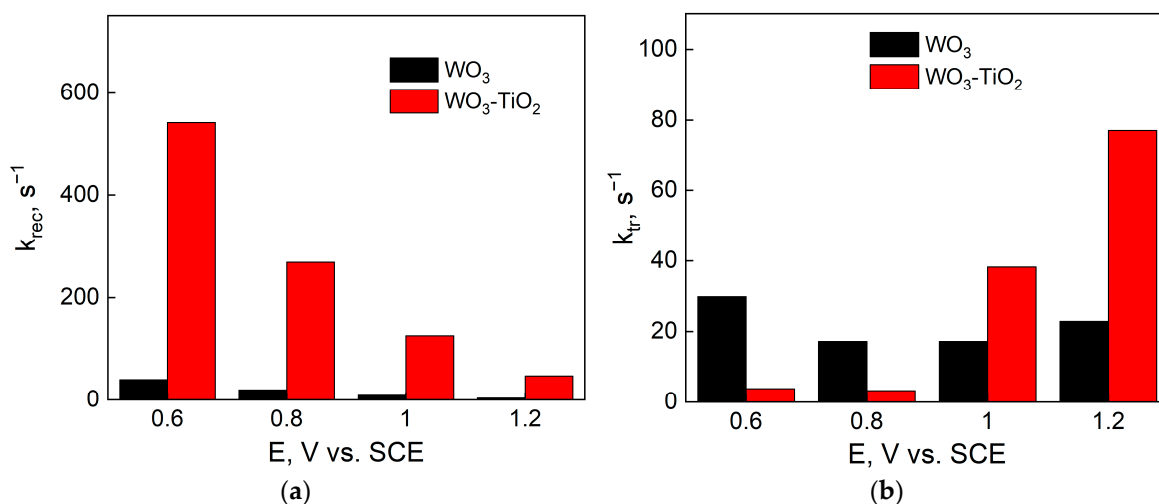


Figure 10. Values of (a) k_{rec} and (b) k_{tr} for WO_3 and $\text{WO}_3\text{-TiO}_2$ films that had been electrodeposited for 5 min.

4. Conclusions

In this study, WO_3 and composite $\text{WO}_3\text{-TiO}_2$ films were prepared by electrodeposition from an acidic peroxy-tungstate precursor solution containing suspended anatase TiO_2 nanoparticles for the formation of the composite. The annealed films were found to be crystalline, with $\text{WO}_3\text{-TiO}_2$ having a distinct monoclinic WO_3 structure, but plain WO_3 displaying characteristics of hydrate formation. XPS showed the dominance of W^{6+} in both samples. In addition, the inclusion of Ti^{4+} and a small amount of Ti^{3+} was proven by deconvoluting the Ti 2p core level spectra. The films prepared in this study were found to be photoelectrochemically active, and $\text{WO}_3\text{-TiO}_2$ generated significantly larger photocurrent magnitudes compared to the WO_3 alone. However, the $\text{WO}_3\text{-TiO}_2$ composite photocurrents possessed considerable recombination at and near open circuit conditions. While the overall transfer efficiency is higher for WO_3 , applying a bias potential resulted in a significant increase in the OER current density of the $\text{WO}_3\text{-TiO}_2$ composite: it is three times higher at an applied potential of 1.2 V vs. SCE, and an associated expected decrease in the electron–hole recombination rate. The implications of these results show that electrodeposition of a $\text{WO}_3\text{-TiO}_2$ composite from an electrolyte containing a peroxy-tungstate precursor and TiO_2 nanoparticles result in significant changes in the material’s structure, morphology, and consequently, PEC activity. The synthesis of composites is facile, they exhibit improved PEC performance as photoanodes when compared to WO_3 , but also suffer from higher photogenerated electron–hole recombination at lower applied potentials.

Author Contributions: Conceptualization, R.L., E.P., N.T. and H.C.; methodology, R.L. and E.P.; formal analysis, R.L.; investigation, R.L., E.P. and N.T.; resources, E.P. and H.C.; data curation, R.L., E.P., N.T. and H.C.; writing—original draft preparation, R.L. and E.P.; writing—review and editing, R.L., E.P., N.T. and H.C.; visualization, R.L.; supervision, E.P. and H.C.; project administration, H.C.; funding acquisition, H.C. All authors have read and agreed to the published version of the manuscript.

Funding: This research has received funding from the European Union’s Horizon 2020 research and innovation program under the Marie Skłodowska-Curie grant agreement No. 778357-SMARTELECTRODES.

It has also received funding from the Research Council of Lithuania (LMTLT), agreement No. S-PD-22-5 (TICAL).

Institutional Review Board Statement: Not applicable.

Informed Consent Statement: Not applicable.

Data Availability Statement: Dataset available on request from the authors.

Conflicts of Interest: The authors declare no conflicts of interest.

References

1. Turner, J.A. Sustainable Hydrogen Production. *Science* **2004**, *305*, 972–974. [[CrossRef](#)] [[PubMed](#)]
2. Bard, A.J.; Fox, M.A. Artificial Photosynthesis: Solar Splitting of Water to Hydrogen and Oxygen. *Acc. Chem. Res.* **1995**, *28*, 141–145. [[CrossRef](#)]
3. Walter, M.G.; Warren, E.L.; McKone, J.R.; Boettcher, S.W.; Mi, Q.; Santori, E.A.; Lewis, N.S. Solar Water Splitting Cells. *Chem. Rev.* **2010**, *110*, 6446–6473. [[CrossRef](#)]
4. Corby, S.; Rao, R.R.; Steier, L.; Durrant, J.R. The Kinetics of Metal Oxide Photoanodes from Charge Generation to Catalysis. *Nat. Rev. Mater.* **2021**, *6*, 1136–1155. [[CrossRef](#)]
5. Holmes-Gentle, I.; Tembhurne, S.; Suter, C.; Haussener, S. Kilowatt-Scale Solar Hydrogen Production System Using a Concentrated Integrated Photoelectrochemical Device. *Nat. Energy* **2023**, *8*, 586–596. [[CrossRef](#)]
6. Fujishima, A.; Honda, K. Electrochemical Photolysis of Water at a Semiconductor Electrode. *Nature* **1972**, *238*, 37–38. [[CrossRef](#)]
7. Thompson, T.L.; Yates, J.T. Surface Science Studies of the Photoactivation of TiO₂ New Photochemical Processes. *Chem. Rev.* **2006**, *106*, 4428–4453. [[CrossRef](#)] [[PubMed](#)]
8. Yagi, M.; Maruyama, S.; Sone, K.; Nagai, K.; Norimatsu, T. Preparation and Photoelectrocatalytic Activity of a Nano-Structured WO₃ Platelet Film. *J. Solid State Chem.* **2008**, *181*, 175–182. [[CrossRef](#)]
9. Amano, F.; Li, D.; Ohtani, B. Tungsten(VI) Oxide Flake-Wall Film Electrodes for Photoelectrochemical Oxygen Evolution from Water. *ECS Trans.* **2010**, *28*, 127–133. [[CrossRef](#)]
10. Bamwenda, G.R.; Arakawa, H. The Visible Light Induced Photocatalytic Activity of Tungsten Trioxide Powders. *Appl. Catal. A Gen.* **2001**, *210*, 181–191. [[CrossRef](#)]
11. González-Borrero, P.P.; Sato, F.; Medina, A.N.; Baesso, M.L.; Bento, A.C.; Baldissera, G.; Persson, C.; Niklasson, G.A.; Granqvist, C.G.; Ferreira Da Silva, A. Optical Band-Gap Determination of Nanostructured WO₃ Film. *Appl. Phys. Lett.* **2010**, *96*, 061909. [[CrossRef](#)]
12. Wu, H.; Xu, M.; Da, P.; Li, W.; Jia, D.; Zheng, G. WO₃-Reduced Graphene Oxide Composites with Enhanced Charge Transfer for Photoelectrochemical Conversion. *Phys. Chem. Chem. Phys.* **2013**, *15*, 16138. [[CrossRef](#)] [[PubMed](#)]
13. Wang, G.; Ling, Y.; Wang, H.; Yang, X.; Wang, C.; Zhang, J.Z.; Li, Y. Hydrogen-Treated WO₃ Nanoflakes Show Enhanced Photostability. *Energy Environ. Sci.* **2012**, *5*, 6180. [[CrossRef](#)]
14. Momeni, M.M.; Nazari, Z. Easy Synthesis of Titania–Tungsten Trioxide Nanocomposite Films by Anodising Method for Solar Water Splitting. *Mater. Sci. Technol.* **2016**, *32*, 855–862. [[CrossRef](#)]
15. Zhang, X.; Liu, F.; Huang, Q.-L.; Zhou, G.; Wang, Z.-S. Dye-Sensitized W-Doped TiO₂ Solar Cells with a Tunable Conduction Band and Suppressed Charge Recombination. *J. Phys. Chem. C* **2011**, *115*, 12665–12671. [[CrossRef](#)]
16. Lv, K.; Li, J.; Qing, X.; Li, W.; Chen, Q. Synthesis and Photo-Degradation Application of WO₃/TiO₂ Hollow Spheres. *J. Hazard. Mater.* **2011**, *189*, 329–335. [[CrossRef](#)]
17. Sotelo-Vazquez, C.; Quesada-Cabrera, R.; Ling, M.; Scanlon, D.O.; Kafizas, A.; Thakur, P.K.; Lee, T.; Taylor, A.; Watson, G.W.; Palgrave, R.G.; et al. Evidence and Effect of Photogenerated Charge Transfer for Enhanced Photocatalysis in WO₃/TiO₂ Heterojunction Films: A Computational and Experimental Study. *Adv. Funct. Mater.* **2017**, *27*, 1605413. [[CrossRef](#)]
18. Zhang, L.; Guo, J.; Hao, B.; Ma, H. WO₃/TiO₂ Heterojunction Photocatalyst Prepared by Reactive Magnetron Sputtering for Rhodamine B Dye Degradation. *Opt. Mater.* **2022**, *133*, 113035. [[CrossRef](#)]
19. Gao, L.; Gan, W.; Qiu, Z.; Zhan, X.; Qiang, T.; Li, J. Preparation of Heterostructured WO₃/TiO₂ Catalysts from Wood Fibers and Its Versatile Photodegradation Abilities. *Sci. Rep.* **2017**, *7*, 1102. [[CrossRef](#)]
20. Székely, I.; Kovács, Z.; Rusu, M.; Gyulavári, T.; Todea, M.; Focșan, M.; Baia, M.; Pap, Z. Tungsten Oxide Morphology-Dependent Au/TiO₂/WO₃ Heterostructures with Applications in Heterogenous Photocatalysis and Surface-Enhanced Raman Spectroscopy. *Catalysts* **2023**, *13*, 1015. [[CrossRef](#)]
21. Castro, I.A.; Byzynski, G.; Dawson, M.; Ribeiro, C. Charge Transfer Mechanism of WO₃/TiO₂ Heterostructure for Photoelectrochemical Water Splitting. *J. Photochem. Photobiol. A Chem.* **2017**, *339*, 95–102. [[CrossRef](#)]
22. Yoon, D.-H.; Biswas, M.R.U.D.; Sakthisabarimoorthi, A. Composite Nanostructures of Black TiO₂/WO₃ on rGO Nanosheets for Photoelectrochemical Water Splitting. *Diam. Relat. Mater.* **2022**, *129*, 109363. [[CrossRef](#)]
23. Liu, K.-I.; Perng, T.-P. Fabrication of Flower-Like WO₃/TiO₂ Core–Shell Nanoplates by Atomic Layer Deposition for Improved Photoelectrochemical Water-Splitting Activity. *ACS Appl. Energy Mater.* **2020**, *3*, 4238–4244. [[CrossRef](#)]

24. Yadav, M.; Yadav, A.; Fernandes, R.; Popat, Y.; Orlandi, M.; Dashora, A.; Kothari, D.C.; Miotello, A.; Ahuja, B.L.; Patel, N. Tungsten-Doped TiO₂/Reduced Graphene Oxide Nano-Composite Photocatalyst for Degradation of Phenol: A System to Reduce Surface and Bulk Electron-Hole Recombination. *J. Environ. Manag.* **2017**, *203*, 364–374. [[CrossRef](#)] [[PubMed](#)]
25. Ki, S.J.; Park, Y.-K.; Kim, J.-S.; Lee, W.-J.; Lee, H.; Jung, S.-C. Facile Preparation of Tungsten Oxide Doped TiO₂ Photocatalysts Using Liquid Phase Plasma Process for Enhanced Degradation of Diethyl Phthalate. *Chem. Eng. J.* **2019**, *377*, 120087. [[CrossRef](#)]
26. Balta, Z.; Simsek, E.B. Insights into the Photocatalytic Behavior of Carbon-Rich Shungite-Based WO₃/TiO₂ Catalysts for Enhanced Dye and Pharmaceutical Degradation. *New Carbon. Mater.* **2020**, *35*, 371–383. [[CrossRef](#)]
27. Patil, S.M.; Deshmukh, S.P.; More, K.V.; Shevale, V.B.; Mullani, S.B.; Dhodamani, A.G.; Delekar, S.D. Sulfated TiO₂/WO₃ Nanocomposite: An Efficient Photocatalyst for Degradation of Congo Red and Methyl Red Dyes under Visible Light Irradiation. *Mater. Chem. Phys.* **2019**, *225*, 247–255. [[CrossRef](#)]
28. Hepel, M.; Hazelton, S. Photoelectrocatalytic Degradation of Diazo Dyes on Nanostructured WO₃ Electrodes. *Electrochim. Acta* **2005**, *50*, 5278–5291. [[CrossRef](#)]
29. Martins, A.S.; Cordeiro-Junior, P.J.M.; Bessegato, G.G.; Carneiro, J.F.; Zandoni, M.V.B.; Lanza, M.R.D.V. Electrodeposition of WO₃ on Ti Substrate and the Influence of Interfacial Oxide Layer Generated in Situ: A Photoelectrocatalytic Degradation of Propyl Paraben. *Appl. Surf. Sci.* **2019**, *464*, 664–672. [[CrossRef](#)]
30. Georgieva, J.; Armyanov, S.; Valova, E.; Philippidis, N.; Poullos, I.; Sotiropoulos, S. Photoelectrocatalytic Activity of Electrosynthesised Tungsten Trioxide- Titanium Dioxide Bi-Layer Coatings for the Photooxidation of Organics. *J. Adv. Oxid. Technol.* **2008**, *11*, 300–307. [[CrossRef](#)]
31. Wang, X.; Li, Z.; Shi, J.; Yu, Y. One-Dimensional Titanium Dioxide Nanomaterials: Nanowires, Nanorods, and Nanobelts. *Chem. Rev.* **2014**, *114*, 9346–9384. [[CrossRef](#)] [[PubMed](#)]
32. Sherkar, T.S.; Momblona, C.; Gil-Escrig, L.; Ávila, J.; Sessolo, M.; Bolink, H.J.; Koster, L.J.A. Recombination in Perovskite Solar Cells: Significance of Grain Boundaries, Interface Traps, and Defect Ions. *ACS Energy Lett.* **2017**, *2*, 1214–1222. [[CrossRef](#)]
33. Rodríguez-Gutiérrez, I.; Djatoubai, E.; Su, J.; Vega-Poot, A.; Rodríguez-Gattorno, G.; Souza, F.L.; Oskam, G. An Intensity-Modulated Photocurrent Spectroscopy Study of the Charge Carrier Dynamics of WO₃/BiVO₄ Heterojunction Systems. *Sol. Energy Mater. Sol. Cells* **2020**, *208*, 110378. [[CrossRef](#)]
34. Pauporté, T. A Simplified Method for WO₃ Electrodeposition. *J. Electrochem. Soc.* **2002**, *149*, C539. [[CrossRef](#)]
35. Meulenkaamp, E.A. Mechanism of WO₃ Electrodeposition from Peroxy-Tungstate Solution. *J. Electrochem. Soc.* **1997**, *144*, 1664–1671. [[CrossRef](#)]
36. Wang, Y.; Meng, Z.; Chen, H.; Li, T.; Zheng, D.; Xu, Q.; Wang, H.; Liu, X.Y.; Guo, W. Pulsed Electrochemical Deposition of Porous WO₃ on Silver Networks for Highly Flexible Electrochromic Devices. *J. Mater. Chem. C* **2019**, *7*, 1966–1973. [[CrossRef](#)]
37. Kim, C.-H.; Kim, Y.-S.; Choi, J.-Y.; Lee, I.-S.; Cha, B.-C.; Kim, D.-W.; Lee, J. Enhancement of Electrochromic Properties Using Nanostructured Amorphous Tungsten Trioxide Thin Films. *RSC Adv.* **2022**, *12*, 35320–35327. [[CrossRef](#)]
38. Boruah, P.J.; Khanikar, R.R.; Bailung, H. Synthesis and Characterization of Oxygen Vacancy Induced Narrow Bandgap Tungsten Oxide (WO_{3-x}) Nanoparticles by Plasma Discharge in Liquid and Its Photocatalytic Activity. *Plasma Chem. Plasma Process* **2020**, *40*, 1019–1036. [[CrossRef](#)]
39. Liu, Y.; Wygant, B.R.; Kawashima, K.; Mabayoje, O.; Hong, T.E.; Lee, S.-G.; Lin, J.; Kim, J.-H.; Yubuta, K.; Li, W.; et al. Facet Effect on the Photoelectrochemical Performance of a WO₃/BiVO₄ Heterojunction Photoanode. *Appl. Catal. B Environ.* **2019**, *245*, 227–239. [[CrossRef](#)]
40. Székely, I.; Kovács, G.; Baia, L.; Danciu, V.; Pap, Z. Synthesis of Shape-Tailored WO₃ Micro-/Nanocrystals and the Photocatalytic Activity of WO₃/TiO₂ Composites. *Materials* **2016**, *9*, 258. [[CrossRef](#)]
41. Sun, H.; Song, F.; Zhou, C.; Wan, X.; Jin, Y.; Dai, Y.; Zheng, J.; Yao, S.; Yang, Y. Lattice-Water-Induced Acid Sites in Tungsten Oxide Hydrate for Catalyzing Fructose Dehydration. *Catal. Commun.* **2021**, *149*, 106254. [[CrossRef](#)]
42. Zhou, Z.; Chen, Z.; Ma, D.; Wang, J. Porous WO₃·2H₂O Film with Large Optical Modulation and High Coloration Efficiency for Electrochromic Smart Window. *Sol. Energy Mater. Sol. Cells* **2023**, *253*, 112226. [[CrossRef](#)]
43. Martín, A.J.; Maffiotte, C.; Chaparro, A.M. Mechanisms for the Growth of Thin Films of WO₃ and Bronzes from Suspensions of WO₃ Nanoparticles. *ECS Trans.* **2015**, *64*, 43–56. [[CrossRef](#)]
44. Mineo, G.; Ruffino, F.; Mirabella, S.; Bruno, E. Investigation of WO₃ Electrodeposition Leading to Nanostructured Thin Films. *Nanomaterials* **2020**, *10*, 1493. [[CrossRef](#)]
45. Yang, B.; Miao, P.; Cui, J. Characteristics of Amorphous WO₃ Thin Films as Anode Materials for Lithium-Ion Batteries. *J. Mater. Sci: Mater. Electron.* **2020**, *31*, 11071–11076. [[CrossRef](#)]
46. Nguyen, H.T.T.; Truong, T.H.; Nguyen, T.D.; Dang, V.T.; Vu, T.V.; Nguyen, S.T.; Cu, X.P.; Nguyen, T.T.O. Ni-Doped WO₃ Flakes-Based Sensor for Fast and Selective Detection of H₂S. *J. Mater. Sci: Mater. Electron.* **2020**, *31*, 12783–12795. [[CrossRef](#)]
47. Vasilopoulou, M.; Soultati, A.; Georgiadou, D.G.; Stergiopoulos, T.; Palilis, L.C.; Kennou, S.; Stathopoulos, N.A.; Davazoglou, D.; Argitis, P. Hydrogenated Under-Stoichiometric Tungsten Oxide Anode Interlayers for Efficient and Stable Organic Photovoltaics. *J. Mater. Chem. A* **2014**, *2*, 1738–1749. [[CrossRef](#)]
48. Wei, Z.; Zhao, M.; Yang, Z.; Duan, X.; Jiang, G.; Li, G.; Zhang, F.; Hao, Z. Oxygen Vacancy-Engineered Titanium-Based Perovskite for Boosting H₂O Activation and Lower-Temperature Hydrolysis of Organic Sulfur. *Proc. Natl. Acad. Sci. USA* **2023**, *120*, e2217148120. [[CrossRef](#)] [[PubMed](#)]

49. Malikov, I.F.; Lyadov, N.M.; Salakhov, M.K.; Tagirov, L.R. Anion Doping of Tungsten Oxide with Nitrogen: Reactive Magnetron Synthesis, Crystal Structure, Valence Composition, and Optical Properties. *Crystals* **2024**, *14*, 109. [[CrossRef](#)]
50. Frankcombe, T.J.; Liu, Y. Interpretation of Oxygen 1s X-ray Photoelectron Spectroscopy of ZnO. *Chem. Mater.* **2023**, *35*, 5468–5474. [[CrossRef](#)]
51. Xu, Y.; Wu, S.; Wan, P.; Sun, J.; Hood, Z.D. Introducing Ti^{3+} Defects Based on Lattice Distortion for Enhanced Visible Light Photoreactivity in TiO_2 Microspheres. *RSC Adv.* **2017**, *7*, 32461–32467. [[CrossRef](#)]
52. Li, J.; Li, W.; Dong, H.; Li, N.; Guo, X.; Wang, L. Enhanced Performance in Hybrid Perovskite Solar Cell by Modification with Spinel Lithium Titanate. *J. Mater. Chem. A* **2015**, *3*, 8882–8889. [[CrossRef](#)]
53. Sun, S.; Li, H.; Xu, Z.J. Impact of Surface Area in Evaluation of Catalyst Activity. *Joule* **2018**, *2*, 1024–1027. [[CrossRef](#)]
54. Diao, J.; Yuan, W.; Qiu, Y.; Cheng, L.; Guo, X. A Hierarchical Oxygen Vacancy-Rich WO_3 with “Nanowire-Array-on-Nanosheet-Array” Structure for Highly Efficient Oxygen Evolution Reaction. *J. Mater. Chem. A* **2019**, *7*, 6730–6739. [[CrossRef](#)]
55. Le Formal, F.; Sivula, K.; Grätzel, M. The Transient Photocurrent and Photovoltage Behavior of a Hematite Photoanode under Working Conditions and the Influence of Surface Treatments. *J. Phys. Chem. C* **2012**, *116*, 26707–26720. [[CrossRef](#)]
56. Ponomarev, E.A.; Peter, L.M. A Generalized Theory of Intensity Modulated Photocurrent Spectroscopy (IMPS). *J. Electroanal. Chem.* **1995**, *396*, 219–226. [[CrossRef](#)]
57. Grigioni, I.; Polo, A.; Nomellini, C.; Vigni, L.; Poma, A.; Dozzi, M.V.; Selli, E. Nature of Charge Carrier Recombination in $CuWO_4$ Photoanodes for Photoelectrochemical Water Splitting. *ACS Appl. Energy Mater.* **2023**, *6*, 10020–10029. [[CrossRef](#)]
58. Nozik, A.J. Photoelectrochemistry: Applications to Solar Energy Conversion. *Annu. Rev. Phys. Chem.* **1978**, *29*, 189–222. [[CrossRef](#)]

Disclaimer/Publisher’s Note: The statements, opinions and data contained in all publications are solely those of the individual author(s) and contributor(s) and not of MDPI and/or the editor(s). MDPI and/or the editor(s) disclaim responsibility for any injury to people or property resulting from any ideas, methods, instructions or products referred to in the content.